

MsMemoryGAN: A Multi-scale Memory GAN for Palm-vein Adversarial Purification

Huafeng Qin, Yuming Fu, Huiyan Zhang, Mounim A. El-Yacoubi, Xinbo Gao, *Fellow, IEEE*, Qun Song, and Jun Wang

Abstract—Deep neural networks have recently achieved promising performance in the vein recognition task and have shown an increasing application trend, however, they are prone to adversarial perturbation attacks by adding imperceptible perturbations to the input, resulting in making incorrect recognition. To address this issue, we propose a novel defense model named MsMemoryGAN, which aims to filter the perturbations from adversarial samples before recognition. First, we design a multi-scale autoencoder to achieve high-quality reconstruction and two memory modules to learn the detailed patterns of normal samples at different scales. Second, we investigate a learnable metric in the memory module to retrieve the most relevant memory items to reconstruct the input image. Finally, the perceptual loss is combined with the pixel loss to further enhance the quality of the reconstructed image. During the training phase, the MsMemoryGAN learns to reconstruct the input by merely using fewer prototypical elements of the normal patterns recorded in the memory. At the testing stage, given an adversarial sample, the MsMemoryGAN retrieves its most relevant normal patterns in memory for the reconstruction. Perturbations in the adversarial sample are usually not reconstructed well, resulting in purifying the input from adversarial perturbations. We have conducted extensive experiments on two public vein datasets under different adversarial attack methods to evaluate the performance of the proposed approach. The experimental results show that our approach removes a wide variety of adversarial perturbations, allowing vein classifiers to achieve the highest recognition accuracy.

Index Terms—Vein recognition, Adversarial attack, Defense, Memory autoencoder.

I. INTRODUCTION

With the rapid development and wide application of Internet technology, information security has received tremendous attention in the past years. Currently, there are various identification/verification technologies such as passwords, cards, fingerprints, and face recognition. Traditional Authentication methods such as passwords, cards, and keys fail to meet the users' requirements in terms of high security and convenience. By leveraging humans' physiological (e.g., face, fingerprint)

or behavioral (e.g., voice, gait) characteristics for identification/verification, biometric technologies have become the solution of choice for authentication, with several systems commercially deployed and numerous biometric modalities extensively investigated over the last years.

Biometrics traits can be broadly categorized into two classes [1] [2]: (1) External modalities, such as face [3], [4], fingerprint [5], [6], and iris [7]; (2) Internal modalities, i.e. finger vein [2], hand vein [8], [9] and palm vein [10]. The external traits are located on the body surface, making the related authentication techniques susceptible to attacks [11]. Facial and fingerprint features, for instance, can be copied without users' consent and the fake version may be employed to fool the face recognition system [12] [13]. The usage of external traits, as a result, raises serious privacy and security issues. Vein biometrics, by contrast, has the following advantages [14] [15]: (1) High security and privacy: Vein blood vessels are hidden inside the body, making them very hard to copy or steal without user awareness. Also, it is difficult to forge a fake vein vessel for spoofing attacks; (2) Liveliness identification: Vein patterns are captured by NIR light with a wavelength of about 850nm. When the NIR light penetrates the skin, the hemoglobin in the blood absorbs more NIR light than surrounding tissues, making veins appear as darker lines or shadows in the acquired images. As hemoglobin only exists in lively bodies, vein biometrics is a natural liveliness identification technology. These reasons explain the dramatic increase of research works on vein recognition in recent years.

A. Motivation

Various approaches [16] have been proposed for vein recognition recently. They can be broadly split into two categories. (1) Traditional vein recognition approaches, i.e. handcrafted-based approaches [17] [18] and traditional machine learning-based approaches [19] [20]. Typical handcrafted approaches employ handcrafted descriptors such as curvature [17], Gabor [18] and LBP [21], to extract the vein patterns. Differently, some works introduced sparse coding [19], low-rank matrix [20] and SVM [22], PCA [23], to automatically learn the vein patterns, avoiding the need of first explicitly extracting some image processing-based features that might discard relevant information about the recognition. (2) Deep learning-based vein recognition approaches. Deep learning (DL) has been proven to be a very powerful tool [24] [25] and shown super feature representation capacity in various computer vision tasks such as image recognition [25], data augmentation [26],

H. Qin, Y. Fu, H.Zhang, and Qun song are with Chongqing Technology and Business University, Chongqing 400067, China (e-mail: qin-huafengfeng@163.com, fym291715@163.com).

M. A. El-Yacoubi is with SAMOVAR, Institut Polytechnique de Paris, 91120 Palaiseau, France (e-mail: mounim.el_yacoubi@telecom-sudparis.eu).

X. Gao is with the Chongqing University of Posts and Telecommunications, Chongqing 400065, China (e-mail: gaodb@cqupt.edu.cn).

J. Wang is with the China University of Mining and Technology, Jiangsu 221116, China (e-mail:WJ999LX@163.com).

Manuscript received September XX, 2023; revised XXXX XX, 201X. (Corresponding author: Qun Song and Huiyan Zhang)

Manuscript received April 19, 2021; revised August 16, 2021.

object tracking [27], image segmentation [28], and so on. It is not surprising then that deep neural networks have been widely applied to vein recognition [29] [30] [31] [32], with promising performance. Although recent works [33] [34] show the domination of DL models in vein recognition tasks, [35] [36] [37] have demonstrated that the DL models are vulnerable to adversarial attacks, which, by adding human-imperceptible perturbations to the original inputs, can mislead classifiers into mis-classifying the perturbed inputs. As shown in Fig. 1, the DL-based classifier Vit [38] is trained based on normal samples and the trained model recognizes a clean sample input with a 98.9% confidence level of belonging to its actual class A. When attacking it through an adversarial generator FGSM [36] by adding adversarial perturbations, however, the resulting adversarial sample is misclassified into class B with a high confidence level (80.8%), even though the perturbation noise is nonperceivable to a human observer. It is possible, therefore, that the attacker intentionally modified data to access genuine users' IDs, resulting in a significant degradation of vein recognition systems' security.

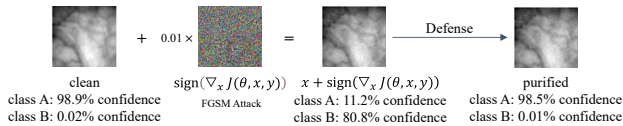


Fig. 1: Adversarial attack results. The perturbation is generated by FGSM attack [36] with Vit [38] classifier. Class A represents the correct class and class B represents the incorrect class. The confidence score of the original image belongs to class A is 98.9%, after adding perturbations to the original image, the resulting adversarial image is classified to class A with a confidence score of 11.2% while it is misclassified to class B with 80.8% probability. After feeding it into our model for purification, the confidence of the resulting purifier images belonging to class A is increased to 98.5%

To overcome this problem, some researchers have developed various approaches [39] [40] to defend deep learning-based recognition models against adversarial attacks. For the same purpose, Li et. al [1] made a first attempt to propose a transformer-based defense GAN, named VeinGuard, for vein adversarial perturbation purification. In [1], a purifier consisting of a trainable residual network and a pre-trained generator was trained by minimizing the reconstruction error, to remove a wide variety of adversarial perturbations. The purifier can be seen as an AutoEncoder(AE) [41] as the trainable residual network and the pre-trained generator can be treated as an encoder and a decoder, respectively. AE [41] is a powerful model for learning high-dimensional data representations in an unsupervised setting. The encoding acts essentially as an information bottleneck which encourages the network to learn the representative patterns of high-dimensional data. In the adversarial defense context, the AE, usually trained on normal samples by minimizing the reconstruction error, uses the trained model as a purifier to remove perturbations. We expect, generally, that the normal samples can be effectively reconstructed. For adversarial samples, the vein patterns only, and not the perturbations, are usually well reconstructed. In other words, the reconstruction error will be small for normal samples and large for adversarial samples. Recent work [42], however, has implied that sometimes the AEs may have good “generalization” so that they are also capable of well

reconstructing the abnormal samples. The adversarial samples, therefore, may also be well reconstructed by AEs, failing thereby to purify the adversarial perturbations. To mitigate the drawbacks of AEs, a deep autoencoder with a memory module (MemAE) [42] was proposed for anomaly detection. Given an input, MemAE does not directly forward its latent encoding representation into the decoder for reconstruction. Rather, it combines its most relevant items in the memory as its encoding, which is input to the decoder for reconstruction. All the normal samples are used for training, enabling thereby the memory to record the prototypical normal patterns in the normal training data. In the test phase, an abnormal sample is also reconstructed by using fewer patterns from the normal samples. The reconstructed sample, however, tends to be close to the normal data as the adversarial image is reconstructed through a linear combination of normal images. In other words, there is a large reconstruction error for abnormal samples, which can be used as a criterion to detect the anomalies. Memory-based approaches have recently been applied to anomaly detection [42] [43] and shown state-of-the-art performance.

B. Our work

Inspired by Memory-based approaches' success in anomaly detection, we propose a multi-scale memory-augmented GAN (MsMemoryGAN) to defend the vein recognition model against adversarial perturbation attacks. First, we propose a multi-scale memory-augmented autoencoder to reconstruct the input images with high quality by modeling multi-scale hierarchical features. Then we combine the autoencoder with a discriminator to form MsMemoryGAN, where the goal of the autoencoder is to reconstruct the input samples with high quality so that the discriminator is unable to distinguish between reconstructed and real samples, and the goal of the discriminator is to correctly judge reconstructed and real samples. Secondly, a learnable metric is investigated to compute the correlation between the features extracted by the encoder and prototypical normal patterns in the memory module. For reconstruction, based on the resulting correlation, the most relevant patterns in the memory to the input are searched as the input representation. Finally, we combine the perceptual loss and pixel loss for model training to reconstruct high-quality images. This reconstruction image is taken as the purified version of the input and is fed to the deep learning-based classifier for vein recognition. The main contributions of our work can be summarized as follows:

(1) We introduce the memory concept in the vein biometrics context to defend deep learning-based vein recognition models against adversarial palm-vein image attacks, and propose a Multi-scale Memory-augmented Autoencoder to filter adversarial perturbations.

(2) We further design a GAN framework (MsMemoryGAN) which consists of our proposed multi-scale memory-augmented autoencoder and a patch-based discriminator. Furthermore, adversarial loss and perceptual loss are incorporated into the training stage to enhance the quality of the reconstructed images.

(3) We design a learnable metric to learn the correlation between the features extracted by the encoder and the normal patterns in the memory module.

(4) We have conducted extensive experiments on two public palm vein datasets to assess the proposed MsMemoryGAN. The results show that MsMemoryGAN can filter the perturbations and allow the vein recognition model to achieve state-of-the-art results under different adversarial attacks.

II. RELATED WORKS

A. Traditional Vein Recognition Algorithms

Traditional vein recognition algorithms can be categorized into hand-designed methods and traditional machine learning (ML) algorithms. The former directly extracts handcrafted features from images for classification. Miura et al. [17], for example, computed the local maximum curvature of the cross-sectional contour of a vein image. In 2021, Li et al. [44] proposed a novel compact multi-representation feature to describe the informative vein features in local patches for finger-vein feature representation. For traditional ML algorithms, Veluchamy et al. [22] proposed a k -SVM technique for finger-vein identification, while Nurul et al. [23] proposed a new filter CCA which takes into account the basic features of the image. Similarly, Lu et al. [20] proposed a low-rank representation to extract as much noise-free discriminative information as possible from finger vein images.

B. Deep learning-based Vein Recognition Algorithms

Deep learning (DL) models have shown powerful feature representation capacity and have been successfully applied in various fields such as image recognition [25], data augmentation [26], object tracking [27], image segmentation [28] and so on. DL has also become the dominant approach for vein recognition. Das et al. [45], for instance, proposed a CNN to achieve stable and high finger vein recognition, while Yang et al. [29], proposed FV-GAN, a new method for finger vein extraction and verification using GANs. Yang et al. [30] then proposed FVRAS-Net, a lightweight CNN integrating both the recognition task and the anti-spoofing task. Qin et al. [10] proposed a single-sample single-person (SSPP) palm vein recognition method, while Pan et al. [31] designed a multiscale deep representation aggregation model for vein recognition. In 2021, Lu et al. [32] proposed a visual transformer (Vit) for finger vein recognition, while, in the same year, Wang et al. [46] a multi-receiver field bilinear convolutional NN for the same task, and Hou et al. [47] proposed a new loss function, called the inverse cosine center loss, to improve the discriminative power of CNNs. In 2022, Shaheed et al. [48] proposed a pre-trained model based on depth-separable convolutional layers for vein recognition. In 2023, Zhang et al. [49] proposed a lightweight model and a feature integration model to save learning time while achieving high accuracy.

C. Defense Methods

To improve the security of vein recognition systems, some researchers have investigated various defense approaches such

as template protection [50] [51] and fake vein detection [52]. Qiu et al., for instance, [52] proposed a novel finger vein attack detection scheme, combining total variation regularization and local binary pattern (LBP) descriptors to improve discrimination and generalization. Lu et al. [50] blended 2DPalmHash Code (2DPHC), a cancelable biometric scheme, and Fuzzy Vault primitive to jointly protect palmprint templates, while Shao et al. [51] proposed a chaotic map-based finger vein template protection method.

While DL models have been widely applied recently for vein recognition, existing studies have shown that classification models relying solely on DL are vulnerable to adversarial sample attacks [35]. An attacker can attack a DL model through white-box attacks such as FSGM [36] and PGD [37] or black-box attacks such as HSJA [53] and SPSA [54]. The aforementioned defense methods, however, have not yet been defended against such attacks. To overcome this problem, numerous adversarial defense methods have been proposed. Meng et al., for instance, proposed MagNet [55], a framework for defense against adversarial examples of NN classifiers. Song et al. devised a method named PixelDefend [56] to purify images by restoring perturbed images, while Samangouei et al. proposed DefenseGAN [40], a defense framework that utilizes a generative model to protect a deep NN from attacks. Inspired by the recent success of Diffusion models in the field of image generation, [39] introduced a diffusion model for defense by adding Gaussian noise to an attacked image, and then performing a pre-trained inverse diffusion process to recover clean samples. To improve the security of the vein recognition system, Li et al. proposed VeinGuard [1], a model to defend vein classifiers against adversarial vein image attacks.

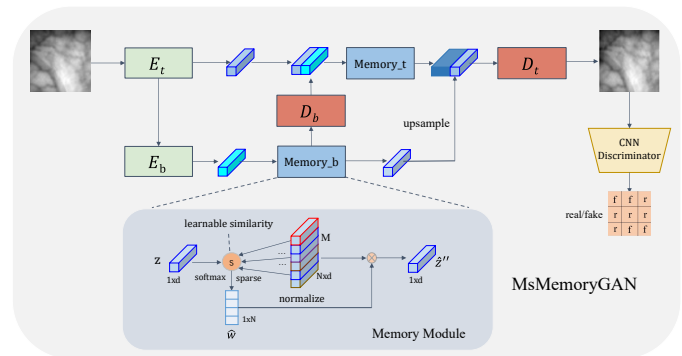


Fig. 2: The architecture of the proposed MsMemoryGAN

III. METHODS

Memory based autoencoders [42] [43] [57] [58] have been extensively used for anomaly detection. The original MemAE consists of an encoder that encodes the input into a latent hidden vector, a memory module that retrieves, from the memory, the most relevant entries of the encoder's output to the entries by an attention-based addressing algorithm, and a decoder network to reconstruct the original image. These models suffer from the following problems: (1) Models are trained with a pixel loss such as the L_2 paradigm to calculate the reconstruction error between pixels. Per-pixel

loss, however, does not capture perceptual differences between output and ground-truth images [59], which leads to a blurred reconstructed image; (2) They employ handcrafted metrics such as *cosine* similarity to retrieve the memory items that are most similar to latent vector z to obtain its representation. These handcrafted metrics may not effectively compute the difference between two latent vectors; (3) As existing approaches process the image at a single scale, they fail to capture local information, such as texture, and global information, such as object shape and geometry, resulting in low-quality images. To defend deep NN-based vein classifiers against adversarial attacks, we propose MsMemoryGAN, a new multi-scale Memory-augmented autoencoder-based defense model to reconstruct clear original images. First, we investigate a multi-scale hierarchical autoencoder to learn the global and local information. Specifically, a top encoder aims to model global information, while a bottom encoder, conditioned on the top latent code is responsible for representing local details. For image reconstruction, the decoder takes both latent codes as input. Second, we propose an improved memory module to retrieve the most relevant items in the memory via a learnable metric. Finally, we introduce a perceptual loss and an adversarial loss, instead of the $L2$ loss, for reconstruction. The encoder and decoder are trained to minimize the reconstruction error, while the memory contents are simultaneously encouraged to record the prototypical elements of the encoded normal data, to obtain a low average reconstruction error. During the test, the model merely uses a limited number of the normal patterns recorded in the memory to perform the reconstruction. As a result, we usually get small reconstruction errors for normal samples and large errors for adversarial samples. In other words, our approach is capable of purifying the perturbations from adversarial samples.

A. Multi-Scale Memory AutoEncoder

To purify adversarial perturbations, we propose a multi-scale Memory AutoEncoder, as shown in Fig. 2, which consists of two memory modules, two encoders modules, and two decoders modules. The two encoders encode the input image at two scales to obtain the local details and global information. The memory modules aim to retrieve the most relevant patterns in the memory for input, to obtain its latent representation for reconstruction. The two decoders are responsible for reconstructing the image from the resulting latent representation. Let $x \in \mathbb{R}^{H \times W \times C}$ be a normal vein sample, where W and H are the input image width and height, and C is the number of channels. As shown in Fig. 3(a), the top encoder E_t includes seven convolutional layers, followed by a Relu activation function. The first two convolutional layers perform convolutional operations with a stride of 2, which is equivalent to transform and downsample the input image by a factor of 4. The bottom encoder (Fig.3(b)) E_b consists of six convolutional layers. As the first layer includes a convolutional operator with a stride of 2, the input image is subject to downsampling with a factor of 2. Taking x as the input, the top encoder outputs the local detail feature representation $z_t \in \mathbb{R}^{\frac{H}{4} \times \frac{W}{4} \times C_t}$, which is further fed to the bottom encoder to learn global feature

representation $z_b \in \mathbb{R}^{\frac{H}{8} \times \frac{W}{8} \times C_b}$. The feature representations are computed by Eq. (1) and Eq. (2):

$$z_t = E_t(x), \quad (1)$$

$$z_b = E_b(z_t), \quad (2)$$

where E_t and E_b denote the top encoder and bottom encoder, as shown in Fig. 3. The bottom latent code z_b is mapped to

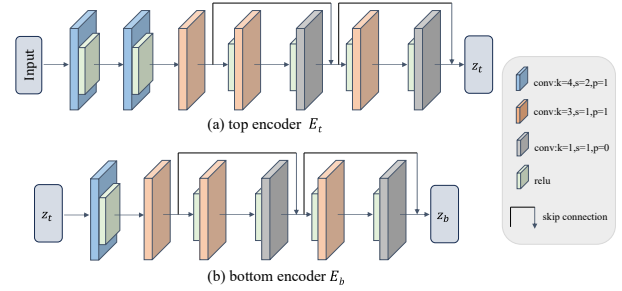


Fig. 3: The architecture of top encoder (a) and bottom encoder (b). The former consists of seven convolutional layers while the latter includes six convolutional layers. Some layers in both encoders are stacked with residual connections. The top encoder transforms and downsamples the image by a factor of 4, while the bottom encoder transforms and downsamples the image by a factor of 2.

a new feature representation z_{bm} through the bottom memory module $Memory_b$, which is input to the bottom decoder D_b for reconstruction. As shown in Fig. 4(b), the bottom decoder D_b includes a convolutional layer, two residual modules, and a deconvolutional layer with a stride of 2. The bottom decoder D_b transforms and upsamples the input map to get purifying feature map $z'_{bm} \in \mathbb{R}^{\frac{H}{4} \times \frac{W}{4} \times C_t}$, which is calculated by Eq. (3):

$$z'_{bm} = D_b(Memory_b(z_b)), \quad (3)$$

where $memory_b$ is the memory module to purify the adversarial perturbations from the attacked sample, to be detailed in the following section. The resulting feature representation z'_{bm} is combined with latent code z_t in Eq. (1) to obtain the $z_{tf} \in \mathbb{R}^{\frac{H}{4} \times \frac{W}{4} \times 2C_t}$ by Eq. (4):

$$z_{tf} = \text{Concat}[z_t, z'_{bm}], \quad (4)$$

The resulting top feature z_{tf} is then input into the top memory module $Memory_t$ to remove the perturbations of samples and the resulting z_{tm} is obtained by Eq. (5):

$$z_{tm} = Memory_t(z_{tf}), \quad (5)$$

Finally, the purified features z_{tm} and z_{bm} are fused to get the multi-scale hierarchical features $z_{tbf} \in \mathbb{R}^{\frac{H}{4} \times \frac{W}{4} \times 3C_t}$, computed by Eq. (6):

$$z_{tbf} = [\text{Concat}[z_{tm}, \text{deconv}(z_{bm})]], \quad (6)$$

where deconv denotes the inverse convolution operation to upsample z_{bm} . The resulting feature representation z_{tbf} is fed to the top decoder D_t for image reconstruction. The reconstructed image $\bar{x} \in \mathbb{R}^{H \times W \times C}$ is computed by Eq. (7):

$$\bar{x} = D_t(z_{tbf}), \quad (7)$$

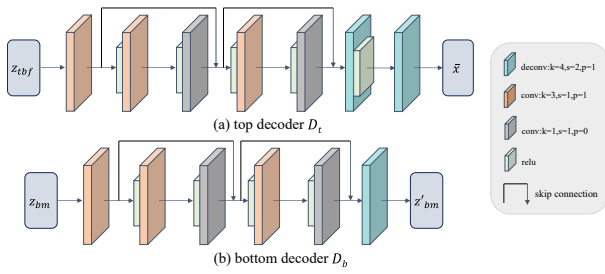


Fig. 4: The architecture of top decoder (a) and bottom decoder (b). The former consists of seven convolutional layers, while the latter includes six convolutional layers. Note that some convolutional layers are stacked with residual connections. The top decoder transforms and upsamples the input vector by a factor of 4, while the bottom decoder transforms and upsamples the input by a factor of 2.

B. Memory module

The Memory module, as in Fig. 2, is proposed to remove the perturbations of vein samples by searching the most relevant latent codes to the given perturbed image from the memory. Different from existing works [42] [43] [57] [58] [60], we design a learnable metric to compute the difference between the input image latent code and the items in memory. As shown in Fig. 5, the proposed memory module includes two convolutional layers and a learnable memory dictionary.

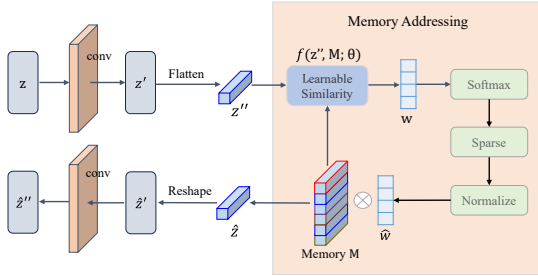


Fig. 5: The memory module architecture. Given a feature vector, we first use a convolutional layer to reduce its dimensionality, and then find the most relevant codes in memory by an MLP network, based on which we can obtain the representations of input on memory. Finally, such representation is input to the convolutional layer for reconstruction.

Memory is a learnable matrix $M \in \mathbb{R}^{N \times d}$ containing N real-valued vectors of fixed dimension d which are updated along with the model. We denote the i_{th} memory item as $m_i \in \mathbb{R}^d$, i.e., the i_{th} row of matrix M , where $i \in [0, N - 1]$. Given a query vector (i.e., an input image latent code) $z \in \mathbb{R}^{W \times H \times C}$, we perform a convolutional operation to obtain $z' \in \mathbb{R}^{W \times H \times c}$, which is flattened to a one-dimensional vector z'' . For convenience, we assume that d has the same dimension as z'' . The memory module employs a soft addressing vector $w \in \mathbb{R}^{1 \times N}$ to obtain \hat{z} by Eq. (8):

$$\hat{z} = wM = \sum_{i=1}^N w_i m_i, \quad (8)$$

where w is a row vector with non-negative elements with their sum equal to 1, and w_i is the i_{th} element of w . It is necessary to access memory M to compute addressing weight w . The hyperparameter N denotes the memory maximum capacity.

The addressing weight vector w is obtained based on z'' and M by Eq. (9):

$$w_i = \frac{\exp(s(z'', m_i))}{\sum_{j=1}^N \exp(s(z'', m_j))}, \quad (9)$$

In existing works [42] [60], the function $s(z, m_i)$ is defined as the cosine similarity between z'' and m_i as Eq. (10):

$$s(z'', m_i) = \frac{z'' m_i^T}{\|z''\| \|m_i\|}, \quad (10)$$

As the cosine similarity is a handcrafted metric, it may not accurately describe the similarity of two vectors. To address this issue, we propose a learnable metric for measuring the difference between a latent code and memory items. In our model, the similarity between z'' and m_i is computed through a multi-layer perception (MLP) in Eq. (11).

$$s(z'', M) = f(z'', M; \theta), \quad (11)$$

where θ is the learnable parameter in MLP f , detailed in Fig. 6:

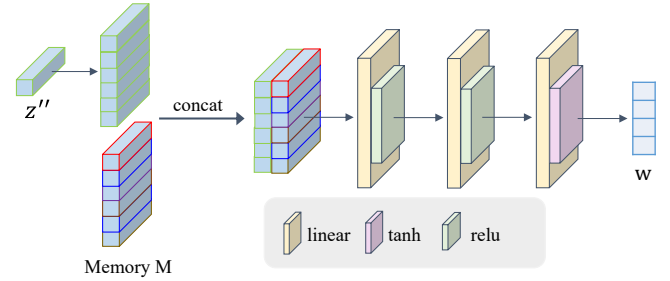


Fig. 6: The MLP network architecture. Given an input vector z'' , we duplicate it N times to obtain N vectors and combine them with memory M (with size N). The resulting feature map passes then through the MLP's three linear layers. The first two linear layers are followed by a ReLU activation function, while the last linear layer is followed by a Tanh activation function. The output $w \in \mathbb{R}^{1 \times N}$ is finally obtained.

Employing a restricted number of normal patterns in the memory to reconstruct the image can help induce a large reconstruction error on an adversarial sample. In other words, the memory autoencoder with only N memory items can not well reconstruct an adversarial sample, leading thereby to the purification of adversarial samples. It is possible, however, that some adversarial samples can be reconstructed well with a complex combination of the memory items based on a dense weight w . To achieve better purification, we propose a sparse addressing approach to reconstruct a sample by only a small number of memory items, as computed by Eq. (12):

$$\hat{w}_i = \text{normalize}\left(\frac{\max(w_i - \gamma, 0) \cdot w_i}{|w_i - \gamma| + \alpha}\right), \quad (12)$$

where $\max(\cdot, 0)$ is the ReLU activation, α is a very small positive number to prevent the denominator from being 0, and γ is the weight threshold. In practice, similar to work [42], the threshold λ is chosen as one of the values in set $[\frac{1}{N}, \frac{3}{N}]$. The normalize is a normalization function. After sparsification, we rewrite Eq. (8) to Eq. (13) as follows:

$$\hat{z} = \hat{w}M = \sum_{i=1}^N \hat{w}_i m_i, \quad (13)$$

where $\hat{w} = [\hat{w}_1, \hat{w}_2, \dots, \hat{w}_N]$. Note that many values of elements in \hat{w} are equal to 0. As shown in Fig. 5, the \hat{z} is subject to reshape to obtain the $\hat{z}' \in \mathbb{R}^{W \times H \times c}$ and finally the output $\hat{z}'' \in \mathbb{R}^{W \times H \times C}$ is obtained by a convolution operation. Sparse addressing encourages the model to construct an image with fewer addressed memory items, to learn more informative representations of normal patterns in memory. This prevents the model from accurately reconstructing the perturbations with lots of dense addressing weights, allowing it thereby to filter adversarial perturbations.

C. Patch-based Discriminator

In this section, We propose, as shown in Fig. 2, a patch-based discriminator to differentiate between real and reconstructed images, compared to the $L2$ pixel loss in [42] [60], the patch-based discriminator [61] is capable of performing strong compression and retaining good perceptual quality in reconstructed images. As shown in Fig.7, the discriminator learns to distinguish whether the patches are from real images or images generated by the corresponding generator.

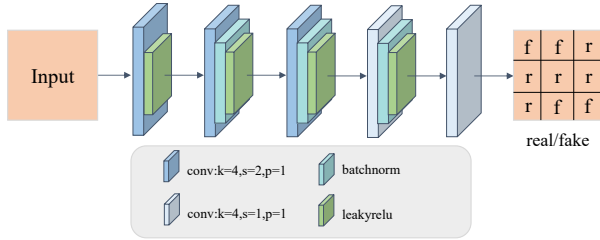


Fig. 7: The architecture of the discriminator. The latter consists of five convolutional layers, where the first only is followed by a LeakyRelu activation function, while the middle three are followed by the batchnorm function and LeakyRelu. The last convolutional layer is used to output a matrix in which each value represents the evaluation value of a small region of the original image.

The discriminator consists of five convolutional layers and three batch normalization layers. In the first four convolutional layers, *leakyrelu* is employed to extract the features. The middle three convolutional layers are followed by normalization layers. Given an input image, the discriminator predicts each of the input patches as real or fake (i.e. generated).

D. Loss Functions

The per-pixel losses in [42] [60] do not capture perceptual and semantic differences between output and original images. To address this limitation, we combine two perceptual losses, i.e. a feature reconstruction loss and an adversarial loss [61] with a pixel loss as a metric to differentiate between real and reconstructed images. Let $\{x_l\}_{l=1}^L$ be a dataset with L images and \bar{x}_l denotes the reconstructed sample from original sample x_l . All losses are introduced as follows.

$L1$ reconstruction loss. Inspired by [61] which showed that the $L1$ distance instead of $L2$ encourages less blurring in reconstructed images, we use the $L1$ metric to measure the reconstruction loss by Eq. (14):

$$L_1(x, \bar{x}) = \|x^L - \bar{x}^L\|_1, \quad (14)$$

Sparse loss: Similar to original MemAE [42], to further promote the sparsity of \hat{w} , we add a sparse regularization

term on memory, by minimizing the entropy of \hat{w} , during the training process, which is computed by Eq. (15):

$$L_s(\hat{w}^l) = \sum_{i=1}^L -\hat{w}_i \cdot \log(\hat{w}_i), \quad (15)$$

In fact, both Eq. (12) and Eq. (15) jointly promote the sparsity of the addressing weights \hat{w} .

Feature reconstruction loss: Rather than exactly matching the pixels of the reconstructed image \bar{x} and the target image x , the perceptual loss computes the distance between the feature representations of the input image and the reconstructed image, which can improve the quality of the reconstructed image [59]. First, we use a pre-trained Resnet18 network on Imagnet [25] to extract feature representations from both the input image and the reconstructed image. Then, the $L2$ loss is employed to compute the distance between the two feature vectors. Let ψ be pre-trained Resnet18 model. $\psi_i(x)$ is the feature map of the i th layer of ψ with an input image x . We obtain feature vector v_i by flattening $\psi_i(x)$. Similarly, we can compute the feature vector \bar{v}_i of the reconstructed image \bar{x} from $\psi(\bar{x})$. The perceptual reconstruction loss between the feature representations is defined by Eq. (16):

$$L_p(x, \bar{x}) = \frac{1}{T} \sum_{i=1}^T \|v_i - \bar{v}_i\|_2^2, \quad (16)$$

where T is the number of feature layers ($T = 5$). Fig. 8 shows the computation process of the perceptual loss.

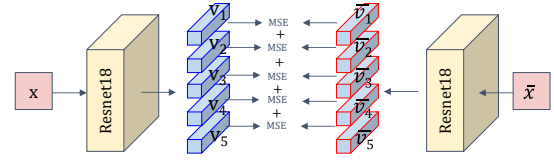


Fig. 8: The original and reconstructed images are fed into resnet18 to obtain the perceptual loss.

Adversarial loss: The classic GAN is difficult to train as the divergences that it typically minimizes are potentially not continuous w.r.t the generator's parameters. To address this problem, we employ the WGAN loss [62] and Hinge GAN loss [63] to train our model, as defined by Eq. (17) and Eq. (18):

$$L_G = -E_{x \sim \mathbb{P}_x} [D(G(x))] \quad (17)$$

$$L_D = E_{x \sim \mathbb{P}_x} [\max(0, 1 - D(x))] + E_{x \sim \mathbb{P}_x} [\max(0, 1 + D(G(x)))] \quad (18)$$

$$L_{adv} = \beta L_G + L_D \quad (19)$$

where \mathbb{P}_x is the data distribution. Note that G is the generator, namely the multi-scale memory AutoEncoder detailed in Section III-A and D is the discriminator, as shown in Fig. 7. β is an adaptive weight of the adversarial loss of L_G , as computed by Eq. (20):

$$\beta = \frac{\nabla_{G_L}(L_1 + L_p)}{\nabla_{G_L}(L_{adv}) + \sigma} \quad (20)$$

where L_p is the perceptual reconstruction loss and L_{adv} is the adversarial loss, $\nabla_{G_{\mathcal{L}}}(\cdot)$ denotes the gradient of the input w.r.t the last layer \mathcal{L} of decoder D_t in Eq. (7), and $\sigma = 10^{-4}$ is used for stable training.

Finally, we combine Eq. (14), Eq. (15), Eq. (16), and Eq. (19) to obtain the complete objective loss by Eq. (21):

$$L = L_1 + L_p + \alpha L_s + L_{adv}, \quad (21)$$

where α is the weight of the information entropy loss. In our experiments, we experimentally set α to 0.0002.

E. Training and testing

The proposed MsMemoryGAN is trained in an end-to-end manner, i.e., the parameters of all the proposed modules are updated simultaneously by the gradient descent method. During the model training, the inputs are **normal** vein image samples, resulting in the pattern of normal samples stored all over the memory module. The decoder in MsMemoryGAN uses a limited number of memory items to reconstruct normal samples by sparse addressing, which promotes efficient utilization of memory. Minimizing the reconstruction error encourages the memory to record the most representative patterns from the input normal samples. During testing, the normal patterns stored in the memory will be retrieved to represent the feature extracted by the encoder and the decoder will reconstruct original samples by using the represented features. As a result, the normal samples are reconstructed accurately. When taking an adversarial sample as the input, the normal patterns are also retrieved for reconstruction, as no perturbed items exist in the memory module, causing the adversarial sample to be reconstructed back to the relatively normal sample. On the other hand, the perturbations of adversarial samples are usually not well reconstructed by retrieving patterns in the normal samples, thereby purifying the perturbations of the adversarial samples.

IV. EXPERIMENTS AND RESULTS

To evaluate the performance of our approach, we conducted extensive experiments on two public palm vein datasets, TJU_PV dataset [64] and PolyU_MN dataset [65], captured by contactless and contact devices at different times, respectively. First, black-box and white-box adversarial attack methods, namely, FGSM [36], PGD [37], SPSA [54] were used to generate adversarial vein images by adding imperceptible perturbations. We then employed various defense models, namely MemAE [42], MemoryDefense [60], Magnet [55], DefenseGAN [40], VeinGuard [1], and DiffPure [39] to purify the perturbations. For recognition the resulting cleaned images were input to state-of-the-art recognition approaches, namely Res2Net [66], Vit [38], SwinTransformer_v2 [67], FV_CNN [45], PV-CNN [10], FVRAS-Net [30], and Lightweight-CNN [68], as well as DefenseGAN_ModelB [40].

A. Datasets

(1) **TJU_PV**: TJU_PV is a palmprint dataset collected at Tongji University [64], collected in a contactless way at

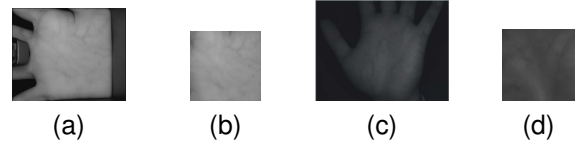


Fig. 9: Preprocessing results: (a) Original image from dataset A; (b) ROI from (a); (c) Original image from dataset B; (d) ROI from (c)

intervals of about 2 months. The collected data are subject to variations such as illumination, translation, rotation, and scale. In each session, each volunteer provides two hands, each of which provides 10 images, resulting in 40 images for each volunteer (10 images \times 2 sessions \times 2 hands). For 300 volunteers, there is thus a total of 12,000 (10 images \times 2 sessions \times 2 hands \times 300 volunteers) palmprint images. If we treat each hand as a category, we obtain a total of 600 categories with 20 images per category. As ROI (region of interest) images were extracted from the original palm-vein images, we directly employ them for model training and evaluation. An original palm-vein image and its normalized ROI are shown in Fig. 9(a) and Fig. 9(b).

(2) **PolyU M_N**: The PolyU Multispectral Palmprint dataset [65], collected at Hong Kong Polytechnic University, uses advanced multispectral imaging equipment for palmprint image acquisition, under blue, green, near-infrared (NIR), and red light illumination. As we focus on palm-vein recognition, only the images collected with NIR light are used in our experiments. The resulting palm-vein dataset comprises 6,000 palm-vein NIR images (250 subjects \times 2 hands \times 12 images) from 250 volunteers, with two hands for each volunteer, and each hand providing 12 images. As the images of each hand are treated as a class, we obtain a total of 500 classes, 12 images per class. Each image is subjected to ROI extraction and alignment by the method in [69]. An original image and its normalized ROI are shown in Fig. 9(c) and Fig. 9(d).

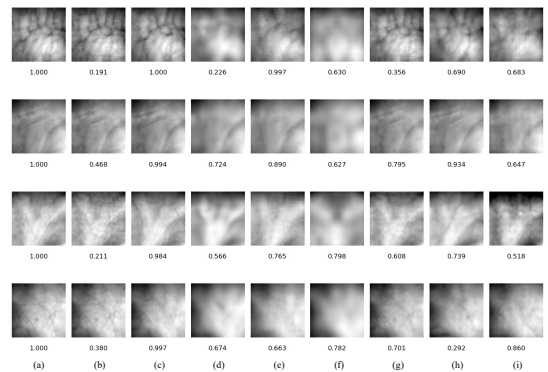


Fig. 10: Reconstruction results of various models on the TJU_PV dataset: (a) Original image; (b) Adversarial image of (a) obtained by FGSM attack; (c) Reconstructed image of (b) using MsMemoryGAN; (d) Reconstructed image of (b) using MemAE; (e) Reconstructed image of (b) using VeinGuard; (f) Reconstructed image of (b) using MemoryDefense; (g) Reconstructed image of (b) using Magnet; (h) Reconstructed image of (b) using DiffPure; (i) Reconstructed image of (b) using DefenseGAN. We list the confidence scores calculated by the Vit model at the bottom of each image

B. Experimental Settings

First, we divide each dataset into training and test sets. Dataset TJU_PV comprises 12,000 images from 600 classes,

TABLE I

Recognition accuracy of different recognition models using different defense methods on the TJU_PV dataset under different strengths of FGSM and PGD white-box attacks.

Method	Attack	Clean	Adversarial	MemAE [42]	MemoryDefense [60]	Magnet [55]	DefenseGAN [40]	VeinGuard [1]	DiffPure [39]	MsMemoryGAN
FV_CNN [45]	FGSM, $L_{\infty}, \epsilon=0.03$	0.953	0.149	0.462	0.570	0.468	0.473	0.605	0.547	0.846
	FGSM, $L_{\infty}, \epsilon=0.05$		0.022	0.499	0.556	0.450	0.407	0.575	0.564	0.791
	PGD, $L_{\infty}, \epsilon=0.03$		0.786	0.469	0.579	0.777	0.357	0.632	0.498	0.840
	PGD, $L_{\infty}, \epsilon=0.05$		0.651	0.475	0.575	0.677	0.352	0.581	0.493	0.835
PV_CNN [10]	FGSM, $L_{\infty}, \epsilon=0.03$	0.998	0.882	0.849	0.755	0.904	0.770	0.843	0.772	0.911
	FGSM, $L_{\infty}, \epsilon=0.05$		0.676	0.810	0.707	0.753	0.696	0.761	0.766	0.953
	PGD, $L_{\infty}, \epsilon=0.03$		0.899	0.838	0.768	0.935	0.764	0.854	0.752	0.984
	PGD, $L_{\infty}, \epsilon=0.05$		0.740	0.818	0.753	0.821	0.707	0.781	0.744	0.977
Lightweight_FVCNN [68]	FGSM, $L_{\infty}, \epsilon=0.03$	0.955	0.691	0.668	0.576	0.890	0.635	0.784	0.672	0.909
	FGSM, $L_{\infty}, \epsilon=0.05$		0.471	0.665	0.557	0.817	0.618	0.719	0.661	0.894
	PGD, $L_{\infty}, \epsilon=0.03$		0.813	0.674	0.576	0.907	0.633	0.852	0.647	0.914
	PGD, $L_{\infty}, \epsilon=0.05$		0.657	0.671	0.578	0.887	0.618	0.769	0.642	0.915
FVRAS_Net [30]	FGSM, $L_{\infty}, \epsilon=0.03$	0.997	0.673	0.749	0.582	0.838	0.673	0.753	0.734	0.966
	FGSM, $L_{\infty}, \epsilon=0.05$		0.407	0.675	0.409	0.620	0.609	0.691	0.719	0.938
	PGD, $L_{\infty}, \epsilon=0.03$		0.789	0.762	0.661	0.946	0.677	0.803	0.724	0.977
	PGD, $L_{\infty}, \epsilon=0.05$		0.553	0.738	0.637	0.891	0.646	0.772	0.706	0.971
DefenseGAN_ModelB [40]	FGSM, $L_{\infty}, \epsilon=0.03$	0.977	0.809	0.709	0.594	0.929	0.727	0.836	0.782	0.939
	FGSM, $L_{\infty}, \epsilon=0.05$		0.685	0.701	0.572	0.902	0.719	0.714	0.770	0.930
	PGD, $L_{\infty}, \epsilon=0.03$		0.833	0.709	0.599	0.939	0.723	0.847	0.771	0.944
	PGD, $L_{\infty}, \epsilon=0.05$		0.687	0.712	0.569	0.936	0.714	0.735	0.762	0.944
Res2Net50 [66]	FGSM, $L_{\infty}, \epsilon=0.01$	0.978	0.880	0.845	0.806	0.928	0.789	0.879	0.662	0.943
	FGSM, $L_{\infty}, \epsilon=0.015$		0.768	0.735	0.801	0.884	0.766	0.865	0.668	0.932
	PGD, $L_{\infty}, \epsilon=0.01$		0.857	0.830	0.806	0.924	0.777	0.861	0.638	0.942
	PGD, $L_{\infty}, \epsilon=0.015$		0.752	0.819	0.803	0.871	0.744	0.823	0.631	0.933
Vit [38]	FGSM, $L_{\infty}, \epsilon=0.01$	0.973	0.650	0.627	0.706	0.756	0.650	0.737	0.521	0.909
	FGSM, $L_{\infty}, \epsilon=0.015$		0.401	0.513	0.606	0.571	0.611	0.712	0.508	0.903
	PGD, $L_{\infty}, \epsilon=0.01$		0.575	0.621	0.705	0.724	0.619	0.704	0.524	0.906
	PGD, $L_{\infty}, \epsilon=0.015$		0.318	0.511	0.607	0.549	0.694	0.659	0.498	0.906
SwinTransformer_v2 [67]	FGSM, $L_{\infty}, \epsilon=0.01$	0.997	0.564	0.879	0.776	0.802	0.767	0.897	0.762	0.980
	FGSM, $L_{\infty}, \epsilon=0.015$		0.261	0.864	0.775	0.646	0.732	0.806	0.741	0.971
	PGD, $L_{\infty}, \epsilon=0.01$		0.353	0.877	0.776	0.755	0.764	0.884	0.744	0.981
	PGD, $L_{\infty}, \epsilon=0.015$		0.102	0.866	0.776	0.545	0.729	0.878	0.723	0.978
Average / Gain		0.979	0.605	0.708 / 0.103	0.660 / 0.055	0.789 / 0.184	0.661 / 0.056	0.769 / 0.164	0.667 / 0.062	0.927 / 0.322

with each class providing 20 images. For each class, We use 15 images for training and remain 5 for testing. This generates 9,000 images (600 classes \times 15 images) in the training set and 3,000 images (600 classes \times 5 images) in the test set. Similarly, from each hand, 8 images are considered for training and 4 for testing in dataset PolyU_MN, generating thereby a training set with 4000 images (500 classes \times 8 images) and a test set with 2000 images (500 classes \times 4 images). Then, Eight recognition models, namely Res2Net [66], Vit [38], SwinTransformer_v2 [67], FV_CNN [45], PV_CNN [10], FVRAS_Net [30], Lightweight_CNN [68], and DefenseGAN_ModelB [40], are trained on normal images in the training sets. Attack methods, FGSM [36], PGD [37], and SPSA [54] are applied to attack test images. Various defense approaches, namely MemAE [42], MemoryDefense [60], Magnet [55], DefenseGAN [40], VeinGuard [1], and DiffPure [39], as well as our approach, are employed to remove the perturbations. Finally, for comparison, We evaluate the accuracy performance of all recognition models on originally normal (unperturbed) samples, adversarial samples, and purified samples. Noted that most biometric recognition systems require an enrolment process. Therefore, all recognition methods are trained to extract the input features and

the similarity of registrations and test images is computed for recognition. The samples in the training set are treated as registered samples and the samples in the test set are matched for similarity with them.

For our approaches, hyperparameter N is the memory size. The performance of the memory module is not sensitive to the size of N for different datasets [42]. Ideally, a large N is suitable for all datasets. We set it to 1000 for both the TJU_PV and PolyU_MN datasets. The sparsity threshold γ in Eq. (7) is set to $\frac{1}{N}$. For model training, the adaptive moment estimation with weight decay (AdamW) [70] optimizer is employed to model parameter optimization. The initial learning rate is set to 0.001, it will eventually reduce to 0.0001 with a cosine scheduler which has a warmup epoch number of 10, the weight decay is 0.05, and the minibatch size to 60 and 40 for TJU_PV database and VERA_PV database respectively. The maximum number of training epochs is set to 1000. All experiments are implemented on PyTorch with an NVIDIA Tesla A100 80G GPU.

C. Visual assessment

In this section, we visually evaluate the performance of the various defense methods. Specifically, we performed FGSM

attacks [36] with the Vit [38] on the test samples to generate adversarial samples. The resulting images were input into the seven defense models as well as our MsMemoryGAN to obtain the reconstructed images (purified images). We compute the probability of samples belonging to a given class before and after reconstruction. The reconstructed images by these defense approaches and their corresponding prediction scores are shown in Fig. 10. To facilitate comparison, we also show the original vein image.

Comparing Fig. 10(a) and Fig. 10(b), it is hard to differentiate them visually but the accuracy is degraded significantly, which is consistent with the results in Fig. 1. From Fig. 10(a) and Fig. 10(c), we observe that our MsMemoryGAN reconstructs high-quality images, as the purified samples generated by MsMemoryGAN have highly consistent distribution with the original images. For example, the details in the original images are almost all retained in the purified images, with a high resolution (Fig. 10(c)). At the same time, the purified images still have high confidence scores, which implies that our MsMemoryGAN is capable of filtering the perturbation and defending recognition models against adversarial attacks. By contrast, there are large differences between the original images and purified images generated by the other approaches. Specifically, MemAE, MemoryDefense, Magnet, and VeinGuard generate blurred reconstructed images (Fig. 10(d), Fig. 10(f), Fig. 10(g), and Fig. 10(h)), where some vein textures are missing. Comparably, DiffPure achieves better reconstruction, but the reconstructed image (Fig. 10(h)) still shows a different vein distribution w.r.t the original image (Fig. 10(a)). Overall, MsMemoryGAN can reconstruct high-quality images while maintaining high confidence scores for the genuine class and outperforming the other approaches.

D. Quantitative Assessment

1) *White Box Attack Results*: To verify the defense performance of MsMemoryGAN, we report the experimental results of various recognition models under white-box attacks, where the attacker accesses full or partial knowledge of the target model such as the architecture, parameters, inputs, outputs, and even training data to achieve better attacks. White-box attacks usually have a high success rate in attacking recognition systems. In our experiments, we apply state-of-the-art white-box attack models, i.e. FGSM [36] and PGD [37] with parameter ϵ , which is the maximum attack intensity. A larger ϵ results in a stronger attack, but with visible perturbations in the test samples. A smaller ϵ , by contrast, may fail to attack the target model. To effectively test our defense method, we consider different ϵ values, 0.03 and 0.05 for the TJU_PV dataset, and 0.3 and 0.2 for the PolyU M_N dataset. The resulting purified samples are fed to the eight recognition models. The experimental results of various models with original, adversarial, and purified images on the two datasets are shown in Tab. I and Tab. II.

From Table I and Table II, we observe that all recognition models achieve more than 95% accuracy on the TJU_PV dataset and more than 88% accuracy on PolyU M_N. Their accuracy, however, is significantly reduced after the FGSM

[36] and PGD [37] attacks, which demonstrates that the DL-based vein recognition systems are prone to adversarial attacks. This conclusion is consistent with the findings in [36]. After removing the adversarial perturbations from the test samples by existing defense approaches and our MsMemoryGAN, the accuracy is significantly improved, which means that the defense approaches are capable of defending the vein recognition system against adversarial attacks.

We observe that our MsMemoryGAN significantly outperforms existing defense methods in terms of recognition accuracy which reaches the highest accuracies, i.e. 0.981 and 0.982 on the two datasets, which are higher than those reached by MemAE [42], VeinGuard [1], DefenseGAN [40], Magnet [55], MemoryDefense [60], and DiffPure [39], achieving thereby a new state-of-the-art. This performance may be attributed to the following facts:

- The MsMemoryGAN’s encoders extract feature representations at different scales from the images to reconstruct high-quality images. As shown in Fig. 10, the local detail texture and global configurations of vein patterns are retained in the reconstructed images;
- Our learnable metric enables the memory module to effectively find a combination of the most relevant normal patterns for a given input as its purifier version, which will be input into the decoder for reconstruction, thereby filtering perturbations. Also, the multi-scale framework allows the memory module to perform purification at different scales, which effectively removes the perturbations and reconstructs cleaned images;
- We combine feature perceptual losses, image reconstruction loss, and adversarial loss, for MsMemoryGAN training, to promote keeping semantic information in the reconstructed samples, resulting in high recognition accuracy.

By contrast, Magnet [55] achieves promising results but shows poor performance in defending vein recognition models against attacks. This is due to the Magnet being an Autoencoder-based defense model. The Autoencoder aims to obtain a compressed encoding from the input and a decoder reconstructs the data from all the latent codes instead of fewer latent codes, which forces the network to extract the representative patterns of high-dimensional data. Therefore, the Autoencoder sometimes achieves good “generalization” so that it can also reconstruct well the adversarial images, which is supported by [42], [71]. Similarly, VeinGuard is essentially an Autoencoder, so the perturbations may be reconstructed in the purified image, which degrades recognition accuracy. Defense-GAN relies on a traditional GAN which fails to learn an adequate distribution of normal data, which results in low-quality reconstructed images, with larger differences between the reconstructed and the original images (Fig. 10(I)). The memory module in MemAE and MemoryDefense may solve this problem by using a few latent codes in the memory module for reconstruction. However, they only achieve image recognition at a single scale. Moreover, as the pixel loss instead of perceptual loss is used for model training, this results in blurred reconstructed images ((Fig. 10(d)) and (Fig. 10(f))).

TABLE II
Recognition accuracy of different recognition models using different defense methods on PolyU M_N dataset under FGSM and PGD white-box attacks.

Method	Attack	Clean	Adversarial	MemAE [42]	MemoryDefense [60]	Magnet [55]	DefenseGAN [40]	VeinGuard [1]	DiffPure [39]	MsMemoryGAN
FV_CNN [45]	FGSM, $L_{\infty}, \epsilon=0.3$	0.976	0.005	0.460	0.516	0.405	0.583	0.631	0.607	0.780
	PGD, $L_{\infty}, \epsilon=0.3$		0.272	0.550	0.534	0.488	0.594	0.617	0.864	0.867
PV_CNN [10]	FGSM, $L_{\infty}, \epsilon=0.3$	0.993	0.176	0.581	0.651	0.582	0.496	0.896	0.905	0.909
	PGD, $L_{\infty}, \epsilon=0.3$		0.528	0.627	0.734	0.928	0.515	0.834	0.972	0.967
Lightweight_FVCNN [68]	FGSM, $L_{\infty}, \epsilon=0.3$	0.885	0.168	0.320	0.459	0.665	0.429	0.528	0.769	0.807
	PGD, $L_{\infty}, \epsilon=0.3$		0.212	0.310	0.528	0.626	0.512	0.649	0.814	0.848
FVRAS_Net [30]	FGSM, $L_{\infty}, \epsilon=0.3$	0.992	0.714	0.879	0.581	0.788	0.367	0.594	0.916	0.961
	PGD, $L_{\infty}, \epsilon=0.3$		0.880	0.883	0.662	0.920	0.762	0.853	0.957	0.973
DefenseGAN_ModelB [40]	FGSM, $L_{\infty}, \epsilon=0.3$	0.914	0.729	0.778	0.508	0.757	0.585	0.804	0.886	0.881
	PGD, $L_{\infty}, \epsilon=0.3$		0.768	0.768	0.549	0.791	0.553	0.828	0.887	0.906
Res2Net50 [66]	FGSM, $L_{\infty}, \epsilon=0.2$	0.993	0.567	0.679	0.759	0.640	0.752	0.815	0.960	0.961
	PGD, $L_{\infty}, \epsilon=0.2$		0.029	0.650	0.785	0.547	0.738	0.838	0.966	0.968
Vit [38]	FGSM, $L_{\infty}, \epsilon=0.2$	0.900	0.095	0.695	0.494	0.497	0.440	0.637	0.754	0.890
	PGD, $L_{\infty}, \epsilon=0.2$		0.623	0.715	0.550	0.641	0.444	0.649	0.866	0.890
SwinTransformer_v2 [67]	FGSM, $L_{\infty}, \epsilon=0.2$	0.991	0.240	0.877	0.767	0.663	0.706	0.826	0.947	0.974
	PGD, $L_{\infty}, \epsilon=0.2$		0.220	0.891	0.840	0.645	0.716	0.807	0.972	0.982
Average / Gain		0.956	0.389	0.666 / 0.277	0.620 / 0.231	0.661 / 0.272	0.575 / 0.186	0.738 / 0.349	0.878 / 0.489	0.910 / 0.521

TABLE III
Recognition accuracy of various recognition models using different defense strategies on TJU_PV dataset under SPSA black-box attack.

Method	Attack	Clean	Adversarial	MemAE [42]	MemoryDefense [60]	Magnet [55]	DefenseGAN [40]	VeinGuard [1]	DiffPure [39]	MsMemoryGAN
FV_CNN [45]	SPSA, $L_{\infty}, \epsilon=0.1$	0.953	0.718	0.569	0.659	0.668	0.450	0.646	0.514	0.806
PV_CNN [10]	SPSA, $L_{\infty}, \epsilon=0.2$	0.998	0.717	0.756	0.649	0.857	0.709	0.884	0.758	0.953
Lightweight_FVCNN [68]	SPSA, $L_{\infty}, \epsilon=0.1$	0.955	0.741	0.651	0.662	0.879	0.594	0.834	0.651	0.900
FVRAS_Net [30]	SPSA, $L_{\infty}, \epsilon=0.2$	0.997	0.371	0.633	0.672	0.683	0.543	0.756	0.677	0.919
DefenseGAN_ModelB [40]	SPSA, $L_{\infty}, \epsilon=0.1$	0.977	0.770	0.693	0.681	0.839	0.710	0.842	0.768	0.941
Res2Net50 [66]	SPSA, $L_{\infty}, \epsilon=0.1$	0.978	0.739	0.778	0.706	0.856	0.700	0.861	0.614	0.917
Vit [38]	SPSA, $L_{\infty}, \epsilon=0.1$	0.973	0.356	0.512	0.575	0.570	0.408	0.623	0.520	0.881
SwinTransformer_v2 [67]	SPSA, $L_{\infty}, \epsilon=0.1$	0.997	0.761	0.883	0.704	0.899	0.786	0.875	0.768	0.977
Average / Gain		0.979	0.647	0.684 / 0.037	0.664 / 0.017	0.781 / 0.134	0.613 / -0.034	0.790 / 0.143	0.659 / 0.012	0.912 / 0.265

TABLE IV
Recognition accuracy of various recognition models using different defense strategies on PolyU M_N dataset under SPSA black box attack.

Model	Attack	Clean	Adversarial	MemAE [42]	MemoryDefense [60]	Magnet [55]	DefenseGAN [40]	VeinGuard [1]	DiffPure [39]	MsMemoryGAN
FV_CNN [45]	SPSA, $L_{\infty}, \epsilon=0.3$	0.976	0.132	0.392	0.435	0.245	0.598	0.693	0.724	0.834
PV_CNN [10]	SPSA, $L_{\infty}, \epsilon=0.3$	0.993	0.550	0.543	0.594	0.557	0.524	0.654	0.904	0.929
Lightweight_FVCNN [68]	SPSA, $L_{\infty}, \epsilon=0.3$	0.885	0.308	0.499	0.523	0.443	0.467	0.593	0.837	0.851
FVRAS_Net [30]	SPSA, $L_{\infty}, \epsilon=0.3$	0.992	0.733	0.873	0.606	0.771	0.781	0.867	0.970	0.975
DefenseGAN_ModelB [40]	SPSA, $L_{\infty}, \epsilon=0.3$	0.914	0.449	0.757	0.549	0.535	0.503	0.719	0.872	0.886
Res2Net50 [66]	SPSA, $L_{\infty}, \epsilon=0.3$	0.993	0.295	0.457	0.563	0.399	0.336	0.665	0.970	0.963
Vit [38]	SPSA, $L_{\infty}, \epsilon=0.3$	0.900	0.558	0.730	0.590	0.580	0.539	0.677	0.872	0.892
SwinTransformer_v2 [67]	SPSA, $L_{\infty}, \epsilon=0.3$	0.991	0.011	0.877	0.699	0.615	0.495	0.744	0.830	0.969
Average / Gain		0.956	0.380	0.641 / 0.261	0.570 / 0.190	0.518 / 0.138	0.530 / 0.150	0.702 / 0.322	0.872 / 0.492	0.912 / 0.532

To effectively filter the perturbations, the DiffPure model adds noise to adversarial examples by following the forward process with a small diffusion time step and recovering cleaned images by solving the reverse stochastic differential equation (SDE).

It is very difficult, however, to determine the amount of noise to add during the forward process, so the reconstructed image is still blurred, as shown in Fig. 10(h).

2) *Black Box Attack Results*: In this section, we show the experimental results of different recognition models to assess the performance of our approach for black-box attacks, where the attacker cannot directly access the details of the target model and defense strategy, but can only observe and manipulate the model through its inputs and outputs. The attacker, therefore, will use the output of the model for a given input to generate adversarial samples. White-box attack methods, such as FGSM, can be used for black-box attacks, but they often require specially designed alternative models or even access to some of the training data. In recent years, the state-of-the-art SPSA approach [54] was shown to perform an efficient black-box attack on the target model with only a finite number of model queries. In our experiments, we first apply SPSA to generate adversarial samples, which are then purified by the various defense methods. The cleaned images are then input to the recognition models, the recognition accuracy of which on the two datasets are reported in Table III and Table IV, respectively.

From Table III and Table IV, we observe that our MsMemoryGAN still shows the highest performance under black-box attacks, which is consistent with the results in Table I and Table II under white-box attacks. After filtering the perturbations by MsMemoryGAN, the various recognition models obtain a significant accuracy improvement, about 26.5% average improvement on dataset TJU_PV, and about 53.2% improvement on dataset PolyU M_N.

V. CONCLUSION

In this paper, we have proposed MsMemoryGAN, a novel defense model against palm-vein adversarial attacks. First, we proposed a multi-scale AutoEncoder to improve feature representation capacity. Then, we designed a memory module with a learnable metric for memory addressing. Finally, we proposed a perceptual loss and an adversarial loss for training. As our MsMemoryGAN reconstructs an adversarial sample by retrieving its typical normal patterns from memory, it effectively removes adversarial perturbations. Our experiments on two public vein datasets with different attacks demonstrate that our MsMemoryGAN is the best at defending against adversarial attacks and achieves a new state-of-the-art.

REFERENCES

- [1] Yantao Li, Song Ruan, Huafeng Qin, Shaojiang Deng, and Mounim A El-Yacoubi. Transformer based defense gan against palm-vein adversarial attacks. *IEEE Transactions on Information Forensics and Security*, 18:1509–1523, 2023.
- [2] Huafeng Qin and Mounim A. El-Yacoubi. Deep representation-based feature extraction and recovering for finger-vein verification. *IEEE Transactions on Information Forensics and Security*, 12(8):1816–1829, 2017.
- [3] M.A. Turk and A.P. Pentland. Face recognition using eigenfaces. In *Proceedings. 1991 IEEE Computer Society Conference on Computer Vision and Pattern Recognition*, pages 586–591, 1991.
- [4] Licheng Liu, CL Philip Chen, and Shutao Li. Hallucinating color face image by learning graph representation in quaternion space. *IEEE transactions on cybernetics*, 52(1):265–277, 2020.
- [5] A. Jain, Lin Hong, and R. Bolle. On-line fingerprint verification. *IEEE Transactions on Pattern Analysis and Machine Intelligence*, 19(4):302–314, 1997.
- [6] Haozhe Liu, Wentian Zhang, Feng Liu, Haoqian Wu, and Linlin Shen. Fingerprint presentation attack detector using global-local model. *IEEE Transactions on Cybernetics*, 52(11):12315–12328, 2021.
- [7] J. Daugman. How iris recognition works. *IEEE Transactions on Circuits and Systems for Video Technology*, 14(1):21–30, 2004.
- [8] A Kumar and K. V Prathyusha. Personal authentication using hand vein triangulation and knuckle shape. *IEEE Transactions on Image Processing: A Publication of the IEEE Signal Processing Society*, 18(9):2127–36, 2009.
- [9] Di Huang, Yinhang Tang, Yiding Wang, Liming Chen, and Yunhong Wang. Hand-dorsa vein recognition by matching local features of multisource keypoints. *IEEE transactions on cybernetics*, 45(9):1823–1837, 2014.
- [10] Huafeng Qin, Mounim A. El-Yacoubi, Yantao Li, and Chongwen Liu. Multi-scale and multi-direction gan for cnn-based single palm-vein identification. *IEEE Transactions on Information Forensics and Security*, 16:2652–2666, 2021.
- [11] Xuerui Wang, Zheng Yan, Rui Zhang, and Peng Zhang. Attacks and defenses in user authentication systems: A survey. *Journal of Network and Computer Applications*, 188(2):103080, 2021.
- [12] David Menotti, Giovanni Chiachia, Allan Pinto, William Robson Schwartz, Helio Pedrini, Alexandre Xavier Falcão, and Anderson Rocha. Deep representations for iris, face, and fingerprint spoofing detection. *IEEE Transactions on Information Forensics and Security*, 10(4):864–879, 2015.
- [13] Pingping Yu, Jiayu Wang, Ning Cao, and Heiner Dintera. Research on face anti-spoofing algorithm based on image fusion. *Computers, materials and continuums*, 009:000, 2021.
- [14] Jong Min Song, Wan Kim, and Kang Ryoung Park. Finger-vein recognition based on deep densenet using composite image. *IEEE Access*, 7(99):66845–66863, 2019.
- [15] Tarshi Jain and Rajendra Kumar. A study of vein recognition system. *Acta Informatica Malaysia*, 3(1):13–15, 2019.
- [16] Nghi C. Tran and Jia-Ching Wang. A survey of finger vein recognition. In *2021 9th International Conference on Orange Technology (ICOT)*, pages 1–5, 2021.
- [17] Naoto Miura, Akio Nagasaka, and Takafumi Miyatake. Extraction of finger-vein patterns using maximum curvature points in image profiles. *Ice Transactions on Information & Systems*, 90(8):págs. 1185–1194, 2007.
- [18] Wei-Yu Han and Jen-Chun Lee. Palm vein recognition using adaptive gabor filter. *Expert Systems with Applications*, 39(18):13225–13234, 2012.
- [19] Shuyi Li and Bob Zhang. Joint discriminative sparse coding for robust hand-based multimodal recognition. *IEEE Transactions on Information Forensics and Security*, 16:3186–3198, 2021.
- [20] Lu Yang, Gongping Yang, Kuikui Wang, Fanchang Hao, and Yilong Yin. Finger vein recognition via sparse reconstruction error constrained low-rank representation. *IEEE Transactions on Information Forensics and Security*, 16:4869–4881, 2021.
- [21] Haiying Liu, Lingfei Song, Gongping Yang, Lu Yang, and Yilong Yin. Customized local line binary pattern method for finger vein recognition. In *Biometric Recognition: 12th Chinese Conference, CCBP 2017, Shenzhen, China, October 28-29, 2017, Proceedings 12*, pages 314–323. Springer, 2017.
- [22] S Veluchamy and LR Karlmarx. System for multimodal biometric recognition based on finger knuckle and finger vein using feature-level fusion and k-support vector machine classifier. *IET Biometrics*, 6(3):232–242, 2017.
- [23] Nurul Maisarah Kamaruddin and Bakhtiar Affendi Rosdi. A new filter generation method in pcanet for finger vein recognition. *IEEE Access*, 7:132966–132978, 2019.
- [24] Shi Dong, Ping Wang, and Khushnood Abbas. A survey on deep learning and its applications. *Computer Science Review*, 40(1):100379, 2021.
- [25] Alex Krizhevsky, I. Sutskever, and G. Hinton. Imagenet classification with deep convolutional neural networks. *Advances in neural information processing systems*, 25(2), 2012.
- [26] Huafeng Qin, Xin Jin, Yun Jiang, Mounim A. El-Yacoubi, and Xinbo Gao. Adversarial automixup. In *International Conference on Learning Representations*, 2024.
- [27] Luca Bertinetto, Jack Valmadre, Joao F Henriques, Andrea Vedaldi, and Philip HS Torr. Fully-convolutional siamese networks for object tracking. In *Computer Vision—ECCV 2016 Workshops: Amsterdam, The*

- Netherlands, October 8-10 and 15-16, 2016, *Proceedings, Part II 14*, pages 850–865. Springer, 2016.
- [28] Shervin Minaee, Yuri Boykov, Fatih Porikli, Antonio Plaza, Nasser Kehtarnavaz, and Demetri Terzopoulos. Image segmentation using deep learning: A survey. *IEEE Transactions on Pattern Analysis and Machine Intelligence*, 44(7):3523–3542, 2022.
- [29] Wenming Yang, Changqing Hui, Zhiquan Chen, Jing-Hao Xue, and Qingmin Liao. Fv-gan: Finger vein representation using generative adversarial networks. *IEEE Transactions on Information Forensics and Security*, 14(9):2512–2524, 2019.
- [30] Weili Yang, Wei Luo, Wenxiong Kang, Zhixing Huang, and Qiuxia Wu. Fvras-net: An embedded finger-vein recognition and antispoofing system using a unified cnn. *IEEE Transactions on Instrumentation and Measurement*, 69(11):8690–8701, 2020.
- [31] Zaiyu Pan, Jun Wang, Guoqing Wang, and Jihong Zhu. Multi-scale deep representation aggregation for vein recognition. *IEEE Transactions on Information Forensics and Security*, 16:1–15, 2020.
- [32] Huimin Lu, Yupeng Li, Chengcheng Zhao, Weiye Liu, Yang Li, and Ning Ma. A novel finger-vein recognition approach based on vision transformer. In *International Conference on Frontiers of Electronics, Information and Computation Technologies*, pages 1–6, 2021.
- [33] Ziyuan Yang, Lu Leng, and Weidong Min. Downsampling in uniformly-spaced windows for coding-based palmprint recognition. *Multimedia Tools and Applications*, pages 1–16, 2023.
- [34] Ziyuan Yang, Lu Leng, Tengfei Wu, Ming Li, and Jun Chu. Multi-order texture features for palmprint recognition. *Artificial Intelligence Review*, 56(2):995–1011, 2023.
- [35] Kui Ren, Tianhang Zheng, Zhan Qin, and Xue Liu. Adversarial attacks and defenses in deep learning. *Engineering*, 6(3), 2020.
- [36] Ian J Goodfellow, Jonathon Shlens, and Christian Szegedy. Explaining and harnessing adversarial examples. *arXiv preprint arXiv:1412.6572*, 2014.
- [37] Aleksander Madry, Aleksandar Makelov, Ludwig Schmidt, Dimitris Tsipras, and Adrian Vladu. Towards deep learning models resistant to adversarial attacks. In *International Conference on Learning Representations*, 2018.
- [38] Alexey Dosovitskiy, Lucas Beyer, Alexander Kolesnikov, Dirk Weissenborn, Xiaohua Zhai, Thomas Unterthiner, Mostafa Dehghani, Matthias Minderer, Georg Heigold, Sylvain Gelly, et al. An image is worth 16x16 words: Transformers for image recognition at scale. *arXiv 2020. arXiv preprint arXiv:2010.11929*, 2010.
- [39] Weili Nie, Brandon Guo, Yujia Huang, Chaowei Xiao, Arash Vahdat, and Anima Anandkumar. Diffusion models for adversarial purification. *ICML: 16805-16827*, 2022.
- [40] Pouya Samangouei, Maya Kabkab, and Rama Chellappa. Defense-gan: Protecting classifiers against adversarial attacks using generative models. *arXiv preprint arXiv:1805.06605*, 2018.
- [41] Bengio, Yoshua, Courville, Aaron, Vincent, and Pascal. Representation learning: A review and new perspectives. *IEEE Transactions on Pattern Analysis & Machine Intelligence*, 35(8):1798–1828, 2013.
- [42] Dong Gong, Lingqiao Liu, Vuong Le, Budhaditya Saha, Moussa Reda Mansour, Svetha Venkatesh, and Anton Van Den Hengel. Memorizing normality to detect anomaly: Memory-augmented deep autoencoder for unsupervised anomaly detection. In *2019 IEEE/CVF International Conference on Computer Vision (ICCV)*, 2020.
- [43] Yurong Chen, Hui Zhang, Yaonan Wang, Yimin Yang, Xianen Zhou, and QM Jonathan Wu. Mama net: Multi-scale attention memory autoencoder network for anomaly detection. *IEEE Transactions on Medical Imaging*, 40(3):1032–1041, 2020.
- [44] Shuyi Li, Ruijun Ma, Lunke Fei, and Bob Zhang. Learning compact multirepresentation feature descriptor for finger-vein recognition. *IEEE Transactions on Information Forensics and Security*, 17:1946–1958, 2022.
- [45] Rig Das, Emanuela Piciuccio, Emanuele Maiorana, and Patrizio Campisi. Convolutional neural network for finger-vein-based biometric identification. *IEEE Transactions on Information Forensics and Security*, 14(2):360–373, 2018.
- [46] Kaixuan Wang, Guanghua Chen, and Hongjia Chu. Finger vein recognition based on multi-receptive field bilinear convolutional neural network. *IEEE Signal Processing Letters*, 28:1590–1594, 2021.
- [47] Borui Hou and Ruqiang Yan. Arcvein-arccosine center loss for finger vein verification. *IEEE Transactions on Instrumentation and Measurement*, 70:1–11, 2021.
- [48] Kashif Shaheed, Aihua Mao, Imran Qureshi, Munish Kumar, Sumaira Hussain, Inam Ullah, and Xingming Zhang. Ds-cnn: A pre-trained xception model based on depth-wise separable convolutional neural network for finger vein recognition. *Expert Systems with Applications*, 191:116288, 2022.
- [49] Zhongxia Zhang, Zhengchun Zhou, Xue Yang, Hua Meng, and Guohua Wu. Convolutional neural network based on multi-directional local coding for finger vein recognition. *Information Sciences*, 623:633–647, 2023.
- [50] Lu Leng and Andrew Beng Jin Teoh. Alignment-free row-co-occurrence cancelable palmprint fuzzy vault. *Pattern Recognition*, 2015.
- [51] Lei Shao, Hengyi Ren, Lijuan Sun, Chong Han, and Jian Guo. Template protection based on chaotic map for finger vein recognition. *IEEE Transactions on Electrical and Electronic Engineering*, 17(1):82–95, 2022.
- [52] Xinwei Qiu, Wenxiong Kang, Senping Tian, Wei Jia, and Zhixing Huang. Finger vein presentation attack detection using total variation decomposition. *IEEE Transactions on Information Forensics and Security*, 13(2):465–477, 2017.
- [53] Jianbo Chen, Michael I Jordan, and Martin J Wainwright. Hop-skipjumpattack: A query-efficient decision-based attack. In *2020 IEEE Symposium on Security and Privacy (SP)*, pages 1277–1294. IEEE, 2020.
- [54] Jonathan Uesato, Brendan O’donoghue, Pushmeet Kohli, and Aaron Oord. Adversarial risk and the dangers of evaluating against weak attacks. In *International Conference on Machine Learning*, pages 5025–5034. PMLR, 2018.
- [55] Dongyu Meng and Hao Chen. Magnet: a two-pronged defense against adversarial examples. In *Proceedings of the 2017 ACM SIGSAC conference on computer and communications security*, pages 135–147, 2017.
- [56] Yang Song, Taesup Kim, Sebastian Nowozin, Stefano Ermon, and Nate Kushman. Pixeldefend: Leveraging generative models to understand and defend against adversarial examples. *arXiv preprint arXiv:1710.10766*, 2017.
- [57] Hyunjong Park, Jongyoun Noh, and Bumsub Ham. Learning memory-guided normality for anomaly detection. *IEEE CVPR*, 2020.
- [58] Xin Huang, Guangrui Wen, Shuzhi Dong, Haoxuan Zhou, and Xuefeng Chen. Memory residual regression autoencoder for bearing fault detection. *IEEE Transactions on Instrumentation and Measurement*, PP(99):1–1, 2021.
- [59] Justin Johnson, Alexandre Alahi, and Li Fei-Fei. Perceptual losses for real-time style transfer and super-resolution. In *Computer Vision—ECCV 2016: 14th European Conference, Amsterdam, The Netherlands, October 11-14, 2016, Proceedings, Part II 14*, pages 694–711. Springer, 2016.
- [60] Eashan Adhikarla, Dan Luo, and Brian D Davison. Memory defense: More robust classification via a memory-masking autoencoder. *arXiv preprint arXiv:2202.02595*, 2022.
- [61] Phillip Isola, Jun Yan Zhu, Tinghui Zhou, and Alexei A Efros. Image-to-image translation with conditional adversarial networks. *IEEE*, 2016.
- [62] Martin Arjovsky, Soumith Chintala, and Léon Bottou. Wasserstein gan. *arXiv preprint arXiv:1701.07875*, 2017.
- [63] Jae Hyun Lim and Jong Chul Ye. Geometric gan. *arXiv preprint arXiv:1705.02894*, 2017.
- [64] Lin Zhang, Zaixi Cheng, Ying Shen, and Dongqing Wang. Palmprint and palmvein recognition based on dcnn and a new large-scale contactless palmvein dataset. *Symmetry*, 10(4):78, 2018.
- [65] David Zhang, Zhenhua Guo, Guangming Lu, Lei Zhang, and Wangmeng Zuo. An online system of multispectral palmprint verification. *IEEE transactions on instrumentation and measurement*, 59(2):480–490, 2009.
- [66] Shang-Hua Gao, Ming-Ming Cheng, Kai Zhao, Xin-Yu Zhang, Ming-Hsuan Yang, and Philip Torr. Res2net: A new multi-scale backbone architecture. *IEEE transactions on pattern analysis and machine intelligence*, 43(2):652–662, 2019.
- [67] Ze Liu, Han Hu, Yutong Lin, Zhuliang Yao, Zhenda Xie, Yixuan Wei, Jia Ning, Yue Cao, Zheng Zhang, Li Dong, et al. Swin transformer v2: Scaling up capacity and resolution. In *Proceedings of the IEEE/CVF conference on computer vision and pattern recognition*, pages 12009–12019, 2022.
- [68] Jiaquan Shen, Ningzhong Liu, Chenglu Xu, Han Sun, Yushun Xiao, Deguang Li, and Yongxin Zhang. Finger vein recognition algorithm based on lightweight deep convolutional neural network. *IEEE Transactions on Instrumentation and Measurement*, 71:1–13, 2021.
- [69] Huafeng Qin, Mounim A El Yacoubi, Jihai Lin, and Bo Liu. An iterative deep neural network for hand-vein verification. *IEEE Access*, 7:34823–34837, 2019.
- [70] Ilya Loshchilov and Frank Hutter. Fixing weight decay regularization in adam. *abs/1711.05101*, 2018.
- [71] Song Qi. Deep autoencoding gaussian mixture model for unsupervised anomaly detection. In *International Conference on Learning Representations*, 2018.